High areal capacity, long cycle life 4 V ceramic all-solid-state Li-ion batteries enabled by chloride solid electrolytes

Laidong Zhou [1,2], Tong-Tong Zuo [3], Chun Yuen Kwok [1], Se Young Kim[1], Abdeljalil Assoud[1], Qiang Zhang [4], Jürgen Janek [3] and Linda F. Nazar [1,2] ✉

All-solid-state Li batteries (ASSBs) employing inorganic solid electrolytes offer improved safety and are exciting candidates for next-generation energy storage. Herein, we report a family of lithium mixed-metal chlorospinels, $Li_2In_xSc_{0.666-x}Cl_4$ ($0 \leq x \leq 0.666$), with high ionic conductivity (up to $2.0\,mS\,cm^{-1}$) owing to a highly disordered Li-ion distribution, and low electronic conductivity ($4.7 \times 10^{-10}\,S\,cm^{-1}$), which are implemented for high-performance ASSBs. Owing to the excellent interfacial stability of the SE against uncoated high-voltage cathode materials, ASSBs utilizing $LiCoO_2$ or $LiNi_{0.85}Co_{0.1}Mn_{0.05}O_2$ exhibit superior rate capability and long-term cycling (up to 4.8 V versus Li^+/Li) compared to state-of-the-art ASSBs. In particular, the ASSB with $LiNi_{0.85}Co_{0.1}Mn_{0.05}O_2$ exhibits a long life of >3,000 cycles with 80% capacity retention at room temperature. High cathode loadings are also demonstrated in ASSBs with stable capacity retention of $>4\,mAh\,cm^{-2}$ ($\sim190\,mAh\,g^{-1}$).

Rechargeable batteries are key technologies for clean energy storage and electric vehicle applications. However, conventional lithium-ion batteries (LIBs) exploit flammable liquid electrolytes, which leads to safety risks, and a graphite negative electrode, which lowers the energy density compared to a lithium-metal anode[1]. Among the alternatives, all-solid-state Li batteries (ASSBs) using a solid electrolyte (SE) and ideally a lithium-metal anode (or anode-less design[2]) offer the potential to meet the growing demand for high energy density and superior safety energy-storage systems[3,4]. Since a highly conductive SE with a wide electrochemical stability window is a key component to realize the promise of ASSBs, a wide range of new materials have been developed[5–7]. The processing of thin-film SE layers[8] as separators has also attracted great interest for further increasing the energy density of ASSBs. Among the different types of SEs, thiophosphates (sulfides) have attracted great interest over the last decade, due to their often high ionic conductivity ($>10\,mS\,cm^{-1}$) and ductile nature[9,10]. However, because sulfides are oxidized at a low potential (~ 2.5 V versus Li^+/Li)[11–13], they are not electrochemically or chemically compatible with typical 4 V cathode active materials (CAMs; that is, $LiCoO_2$, $LiNi_{1-x-y}Co_xMn_yO_2$)[14]. Coating of CAM particles with an electronically insulating/ionically conductive, chemically compatible material is required to address this problem, which brings a myriad of additional issues. These include the difficulty of finding and processing suitable materials to achieve a homogeneous, functional coating[15–18]. The goal is thus to find SE materials with high ionic conductivity and high voltage stability, along with good ductility.

In 2018, Asano et al. reported that poorly crystalline Li_3YCl_6 exhibits a relatively good ionic conductivity of $0.51\,mS\,cm^{-1}$. They were able to achieve stable cycling of ASSBs using this electrolyte with uncoated $LiCoO_2$ (ref. [19]). Since then, chloride SEs have garnered increasing interest due to their intrinsically high oxidative stability (~4.3 V) and apparent chemical stability with many

CAMs[20]. Several materials, namely semiglassy Li_3ErCl_6 (ref. [21]), Li_3InCl_6 (ref. [22]), $Li_{3-x}M_{1-x}Zr_xCl_6$ (M = Y, Er, Yb)[23,24], Li_xScCl_{3+x}[25], $Li_2Sc_{2/3}Cl_4$ (ref. [26]), poorly crystalline Li_2ZrCl_6 (ref. [27]) and $Li_{3-x}Yb_{1-x}Hf_xCl_6$ (ref. [28]), were reported that exhibit such promising properties. Nonetheless, a very limited number of chloride SEs show ionic conductivity above $1\,mS\,cm^{-1}$, driving an essential search for new materials.

Another major challenge for ASSBs is the moderate CAM loadings that are typically utilized in the literature ($<1.25\,mAh\,cm^{-2}$). To improve energy density, high-loading cathodes (that is, with areal capacities $>3\,mAh\,cm^{-2}$) must be developed to make ASSBs practically competitive with conventional LIBs[29]. However, as the CAM loading increases in ASSBs, the ionic and electronic conduction percolation within the cathode composite declines substantially, leading to poor CAM utilization[30]. Thus cathode composite engineering, along with a highly conductive SE, is needed.

Herein, we report a family of fast Li-ion conducting chlorides, $Li_2In_xSc_{0.666-x}Cl_4$ ($0 < x < 0.666$), which exhibit room temperature ionic conductivity up to $2.0\,mS\,cm^{-1}$. Incorporation of as little as 10 wt% $Li_2In_{1/3}Sc_{1/3}Cl_4$ with bare CAMs forms a cathode composite with excellent electrochemical performance, owing to a low-impedance SE/CAM interface. ASSBs utilizing uncoated $LiCoO_2$ (LCO), $LiNi_{0.6}Co_{0.2}Mn_{0.2}O_2$ (NCM622) and high-Ni $LiNi_{0.85}Co_{0.1}Mn_{0.05}O_2$ (NCM85) at typical cell loading levels of $\sim1.25\,mAh\,cm^{-2}$ exhibit superior rate capability and notably more stable long-term cycling up to 4.8 V versus Li^+/Li, compared with state-of-the-art ASSBs. Furthermore, NCM85 ASSBs show an exceptionally long life at room temperature: up to 3,000 cycles with >80 % capacity retention. LCO ASSBs with CAM loadings up to $52.5\,mg\,cm^{-2}$ ($7\,mAh\,cm^{-2}$) also exhibit very steady long-term cycling with high specific capacity at both room temperature and high temperature (50 °C). NCM85 ASSBs with a high loading of $21.6\,mg\,cm^{-2}$ exhibit a capacity of $>4\,mAh\,cm^{-2}$ ($>190\,mAh\,g^{-1}$)

[1]Department of Chemistry and the Waterloo Institute for Nanotechnology, University of Waterloo, Waterloo, Ontario, Canada. [2]Joint Center for Energy Storage Research, Argonne National Laboratory, Argonne, IL, USA. [3]Institute of Physical Chemistry and Center for Materials Research, Justus Liebig University, Gießen, Germany. [4]Neutron Scattering Division, Oak Ridge National Laboratory, Oak Ridge, TN, USA. ✉e-mail: lfnazar@uwaterloo.ca
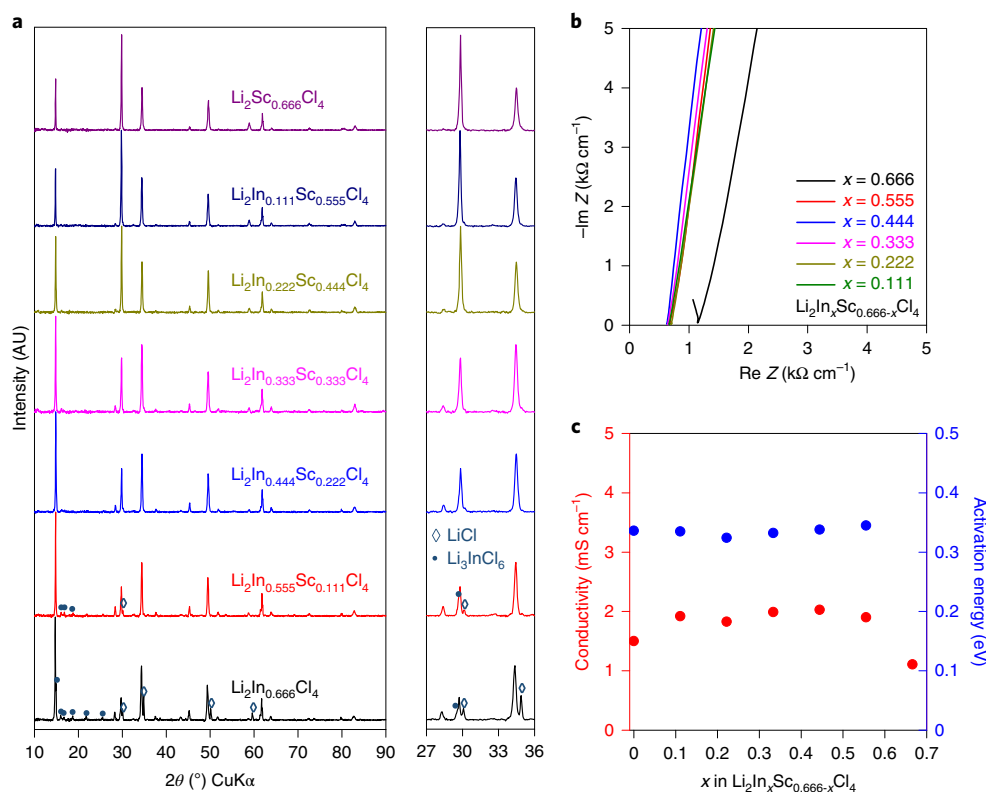
Fig. 1 | X-ray diffraction patterns and Li-ion conductivity of $Li_2In_xSc_{0.666-x}Cl_4$. **a**, X-ray diffraction patterns of $Li_2In_xSc_{0.666-x}Cl_4$ ($0 \leq x \leq 0.666$). **b**, Nyquist plots of $Li_2In_xSc_{0.666-x}Cl_4$ ($0.111 \leq x \leq 0.666$) at room temperature, normalized for the pellet thickness. **c**, Ionic conductivity and activation energy of $Li_2In_xSc_{0.666-x}Cl_4$ ($0 \leq x \leq 0.666$) as a function of nominal In^{3+} content. The ionic conductivity and activation energy values for $x = 0$ were previously reported in ref. [26].

with no fading. These ultra-stable, high-voltage and high-loading solid state cells provide valuable insight into the design and development of ASSBs and may serve as an important point of reference.

Synthesis and characterization of chloride SEs

X-ray diffraction patterns (Fig. 1a) show that the synthesis of $Li_2In_xSc_{0.666-x}Cl_4$ provides an almost phase-pure cubic spinel phase within the solid solution range of $0 \leq x < 0.444$. At higher In^{3+} content ($x \geq 0.555$) the fractions of monoclinic Li_3InCl_6 and LiCl impurities start to increase (Fig. 1a). The ionic conductivity and activation energy were determined with temperature-dependent electrochemical impedance spectroscopy (EIS) measurements (Fig. 1b and Supplementary Fig. 1). The corresponding room-temperature ionic conductivities and activation energies are summarized in Fig. 1c and Supplementary Table 1. All $Li_2In_xSc_{0.666-x}Cl_4$ phases ($0 < x < 0.666$) exhibit high ionic conductivity between 1.83 and 2.03 mS cm^{-1} and a low activation energy of ~0.33 eV (Fig. 1c).

The structure of $Li_2In_{1/3}Sc_{1/3}Cl_4$ from powder neutron diffraction (Fig. 2a and Supplementary Table 2) is similar to that of our previously reported halospinel $Li_2Sc_{2/3}Cl_4$[26], and also contains four Li sites per unit cell, albeit with low occupation. Four Li sites in a spinel structure were also recently reported for the lithiated $Li_4Ti_5O_{12}$ spinel[31]; the metastable intermediate Li sites in $Li_{4+x}Ti_5O_{12}$ ($0 \leq x \leq 3$) lead to excellent Li-ion mobility and allow fast rate capability[32]. In $Li_2In_{1/3}Sc_{1/3}Cl_4$, the edge-sharing (Li4/Sc1/In1) octahedra form a rigid framework, whereas the additional Li-ions are spread over other available octahedral and tetrahedral sites within the lattice (Fig. 2b). The face-sharing Li2 octahedra and Li1 or Li3 tetrahedra with low occupancies (~0.2–0.3) form a three-dimensional (3D) Li-ion diffusion pathway (Fig. 2c,d). Owing to the relatively low activation energy (0.33 eV from EIS measurements) for Li-ion

diffusion and 3D pathways with a considerable site fraction of vacancies that promote Li-ion mobility, a high ionic conductivity of 2.0 mS cm^{-1} was obtained. The electronic conductivity measured (σ_e) by d.c. polarization was 4.7×10^{-10} S cm^{-1} (Supplementary Fig. 2). This σ_e is lower than in the case of other lithium metal chlorides ($1.0–5.4 \times 10^{-9}$ S cm^{-1})[19,22,28], and even one order of magnitude lower than that of $Li_2Sc_{2/3}Cl_4$ ($\sigma_e = 4.2 \times 10^{-9}$ S cm^{-1}; Supplementary Fig. 2). $Li_2In_{1/3}Sc_{1/3}Cl_4$ is, therefore, effectively a Li-ion conductor and an electronic insulator.

At the higher indium content, $Li_2In_{0.444}Sc_{0.222}Cl_4$ shows additional reflections ($Q = 1.1–1.9$ Å^{-1}) in the neutron diffraction pattern, which correspond to a non-spinel phase (Supplementary Fig. 3a). Its high-resolution powder X-ray diffraction pattern (Supplementary Fig. 3b) also reveals reflections at $2\theta = 15–25°$ that are of much lower intensity than in $Li_2In_{1/3}Sc_{1/3}Cl_4$, which are due to monoclinic $Li_3In_{2/3}Sc_{1/3}Cl_6$ (note that the main peaks overlap with spinel reflections). A crystal of $Li_3In_{2/3}Sc_{1/3}Cl_6$ was picked from the two-phase mixture, and its structure was confirmed by single-crystal diffraction measurement (Supplementary Tables 3–5). The refinement yields a lower-than-expected Li content ($Li_{2.18}In_{0.664}Sc_{0.336}Cl_6$) due to poor sensitivity of the X-rays for light lithium atoms, but the In/Sc ratio is as targeted (2:1). The framework of $Li_3In_{2/3}Sc_{1/3}Cl_6$ is identical to monoclinic Li_3ScCl_6 (ref. [33]). One difference between the cubic spinel and monoclinic structures is the fact that the Li/metal site (Li4/Sc1/In1) is shared in the spinel, whereas all of the Li and metal sites are crystallographically distinct in the monoclinic structure (that is, they are ordered) (Supplementary Fig. 4). The ordering is possibly due to the relatively larger ionic radius difference between Li$^+$ (0.76 Å, coordination number (CN) = 6) and In^{3+} (0.8 Å, CN = 6), compared to Sc^{3+} (0.745 Å, CN = 6), which triggers formation of about 40 wt%
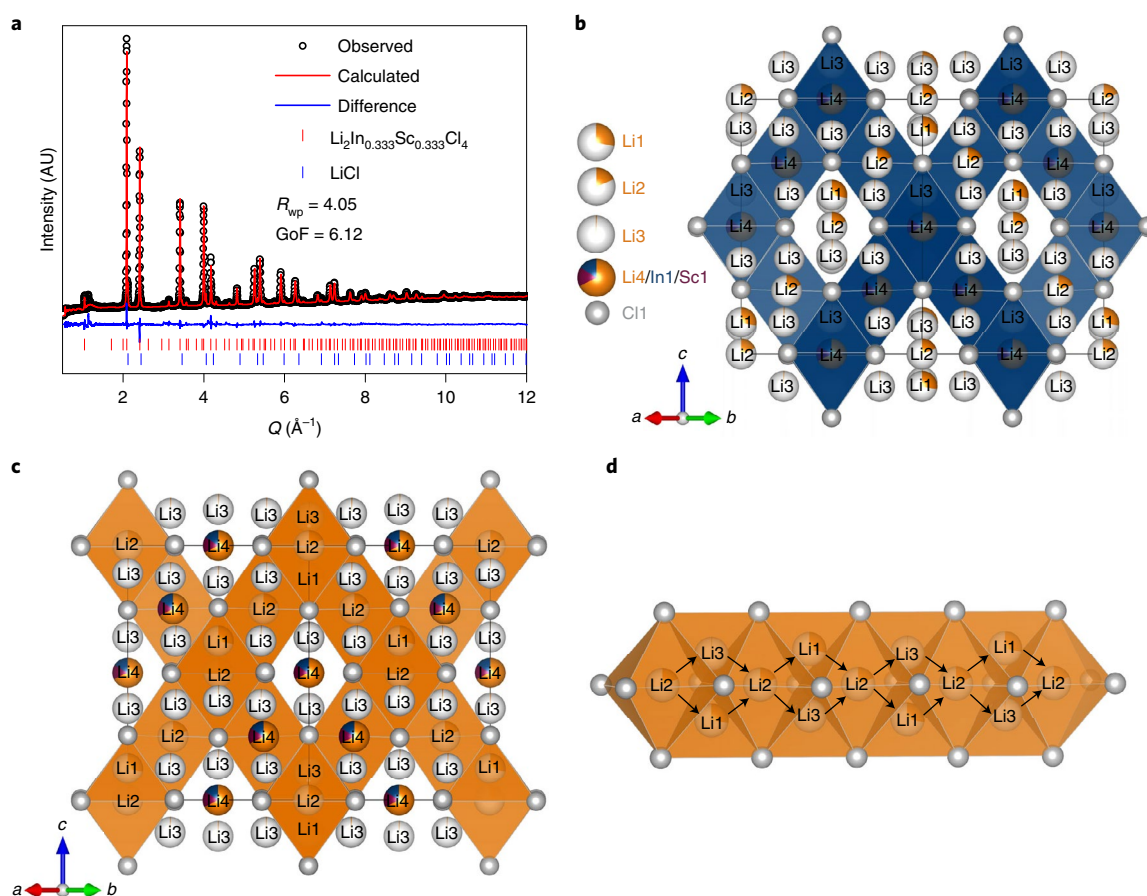
Fig. 2 | Structure of Li₂In₁/₃Sc₁/₃Cl₄ and proposed Li-ion diffusion pathway. a, Time-of-flight neutron diffraction pattern and the corresponding Rietveld refinement of $Li_2In_{1/3}Sc_{1/3}Cl_4$. Experimental data are shown in black circles; the red line denotes the calculated pattern; the difference profile is shown in blue; and calculated positions of the Bragg reflections are shown as red ($Li_2In_{1/3}Sc_{1/3}Cl_4$, 97.424 wt%) and blue (LiCl, 2.576 wt%) vertical ticks. R_{wp} and GoF are the weighted profile R-factor and goodness-of-fit, respectively. **b**, Structure of $Li_2In_{1/3}Sc_{1/3}Cl_4$ from the refinement, showing only the blue Li4/In1/Sc1 octahedral framework. **c**, Structure depicting the face-sharing Li1 tetrahedra and Li2 octahedra that represent the main 3D Li-ion diffusion pathway; Li1 tetrahedra and Li2 octahedra in light orange. **d**, Enlarged Li-ion diffusion pathway through Li2 octahedra passing through Li1 or Li3 tetrahedra.

$Li_3In_{2/3}Sc_{1/3}Cl_6$ in the high-indium content material on slow cooling (see neutron diffraction refinement results in Supplementary Fig. 3a and Supplementary Table 6). As both spinel[26] and monoclinic phases[22,25] reported previously display good ionic conductivities, the two-phase composition with $x = 0.444$ also exhibits a high ionic conductivity of 2.0 mS cm⁻¹ (Fig. 1c).

ASSBs with a typical cell loading of 1.25 mAh cm⁻²

ASSBs using $Li_2In_{1/3}Sc_{1/3}Cl_4$ as the catholyte with uncoated CAMs (bare-LCO, bare-NCM622 or NCM85), and In/InLi as the negative electrode (see cell design in Supplementary Fig. 5), were fabricated to examine the electrochemical performance of $Li_2In_{1/3}Sc_{1/3}Cl_4$. A thin layer of highly conductive argyrodite SE ($Li_{6.7}Si_{0.7}Sb_{0.3}S_5I$)[34] was added on top of the In/InLi to reduce the total cell resistance and prevent reduction of the chloride SE. A layer of $Li_2In_{1/3}Sc_{1/3}Cl_4$ between the negative electrode and the cathode composite served as the separator. The cathode composite typically consisted of 80 wt% CAM and 20 wt% $Li_2In_{1/3}Sc_{1/3}Cl_4$. Figure 3 shows the excellent rate capability of both LCO (Fig. 3a,b) and NCM85 (Fig. 3c,d) ASSBs.

Long-term cycling at a C/5 rate was performed for NCM85 cycled between 2.8 V and 4.3 V versus Li⁺/Li (Fig. 4a and Supplementary Fig. 6a) and NCM622 cycled between 2.8 V and 4.6 V versus Li⁺/Li (Fig. 4b and Supplementary Fig. 6b). Liquid cells with NCM85 or NCM622 cathodes were constructed and cycled under the same conditions as the ASSBs for comparison.

The NCM85 ASSB exhibits only minor capacity fade, maintaining 90% capacity retention over >600 cycles. In contrast, the NCM85 liquid cell shows fast capacity fade with 80% capacity retention over only 100 cycles (Supplementary Fig. 6c,d). Figure 4b and Supplementary Fig. 6b show the capacity retention and voltage profile of the NCM622 ASSB, which achieves up to 194 mAh g⁻¹ and sustains >180 mAh g⁻¹ over 320 cycles. Conversely, the NCM622 liquid cell fades very quickly, and the cell retains a mere 62 mAh g⁻¹ capacity over 150 cycles (Supplementary Fig. 6e,f) owing to the combination of interphase impedance growth on the cathode and Li metal anode, respectively.

NCM85 ASSBs also exhibit stable cycling and very slow capacity fading at high voltage, even at 4.8 V versus Li⁺/Li over >110 cycles, as shown in Fig. 4d,e. The slow capacity fading is not due to SE decomposition (next section) but is probably related to the known structural transformation of high-Ni NCM at high voltage (H2–H3 transition) and O₂ release. The cell maintains 95% capacity retention over 110 cycles, which is superior to the liquid cell performance using an advanced electrolyte[35].

Since a commercial LIB contains more than 90 wt% CAM in the cathode composite, for comparison we also fabricated a NCM85 ASSB with a cathode composite containing 10 wt% chloride SE and 90 wt% NCM85 (Supplementary Fig. 7). The cell exhibits very good cycling behaviour, but slightly lower discharge capacity (180 mAh g⁻¹) compared to the ASSB with 80 wt% NCM85 (Fig. 4a).
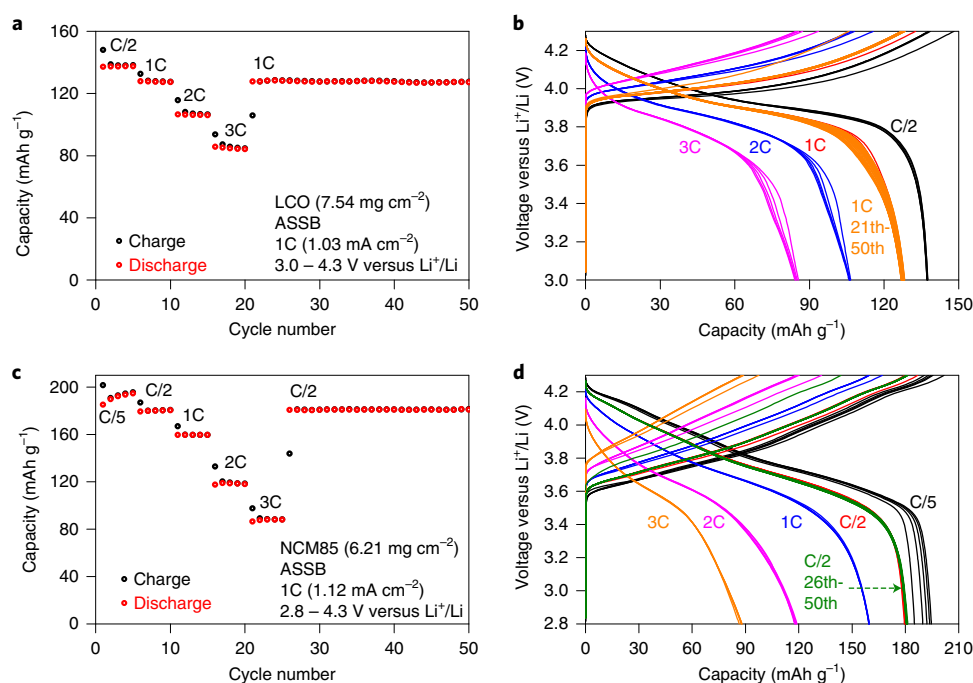
Fig. 3 | Room temperature rate capability of ASSBs. a–d, Charge–discharge capacity as a function of cycle number at different C rates for ASSBs consisting of cathode active materials and 20 wt% $Li_2In_{1/3}Sc_{1/3}Cl_4$ for LCO (**a**) and NCM85 (**c**) and corresponding charge–discharge curves at different C rates for LCO (**b**) and NCM85 (**d**).

We ascribe this to poorer ionic conduction percolation within the cathode composite due to the lower content of SE, which could probably be improved by further nanostructuring the catholyte and optimizing cathode crystallite size and morphology[36,37].

To demonstrate the long-term cycle life of the ASSBs, after the rate cycling studies in Fig. 3d, cycling of the NCM85 ASSBs was continued at a high 3C rate corresponding to charge–discharge in 20 minutes. Over more than 1,000 cycles at room temperature, the NCM85 ASSB exhibits virtually no fading and maintains a capacity of 86 mAh g^{-1}; moreover, the cell sustains >80% retention over 3,000 cycles (Fig. 4c and Supplementary Fig. 8). A second cell was also constructed and exhibited the same excellent long-term cycling stability (Supplementary Fig. 9). At a 2C rate, the cell maintains a high discharge capacity of ~155 mAh g^{-1} and sustains >94% capacity over 1,800 cycles (Supplementary Fig. 10). The overall performance is amongst the best compared with that reported for all-ceramic ASSBs[10,19,22–28,38], as summarized in Supplementary Table 7.

Electrochemical performance of high-loading ASSBs

While the above-mentioned ASSBs exhibit superior electrochemical performance (compared with previously reported results) at typical cathode loadings of 6–8 mg cm^{-2}, it is desirable to increase the loading to provide comparable areal capacities to commercial LIBs (typically >3 mAh cm^{-2})[29]. We note the paucity of data on such cells in the literature[2,10,29,39]. Figure 5a and Supplementary Fig. 11a show the results for high-loading ASSBs (27 mg cm^{-2} LCO; 3.7 mAh cm^{-2}) cycled at a high current density of 1.24 mA cm^{-2} at room temperature. They deliver stable capacity retention and high specific capacity (>3 mAh cm^{-2} and >110 mAh g^{-1} over 180 cycles), albeit with moderately high overpotential under these aggressive conditions. High-loading LCO ASSBs cycled at 50 °C, and even a higher current density of 1.79 mA cm^{-2}, deliver excellent reversible capacity and high specific capacity with much lower overpotential (Fig. 5b and Supplementary Fig. 11b). Furthermore, owing to the high electronic conductivity of LCO, ultra-high-loading ASSBs (52.46 mg cm^{-2}, 7.2 mAh cm^{-2}) deliver

stable areal capacity of 3 mAh cm^{-2} at 25 °C and 4.5 mAh cm^{-2} at 50 °C at a high current density of 1.20 mA cm^{-2} with no capacity fade for over 500 cycles (Fig. 5c and Supplementary Fig. 11c).

Because the battery market is focused on high-Ni NCM-type CAMs, we also benchmarked a high-loading NCM85 ASSB (21.59 mg cm^{-2}). The cell (Fig. 5d,e) delivers an areal capacity of 4.14 mAh cm^{-2} (specific capacity of 192 mAh g^{-1}; very close to the typical value of ~200 mAh g^{-1} observed in liquid LIBs). The high-loading NCM85 ASSBs were repeated twice (22.31 and 22.00 mg cm^{-2} loading, respectively; Supplementary Fig. 12), essentially providing the same results and demonstrating reproducibility. Since using an In/InLi anode will significantly lower the cell energy density, micron-sized prelithiated Si can be used as an alternative negative electrode due to its high electronic conductivity and good mechanical properties. Supplementary Fig. 13 illustrates the fabrication of such an NCM85 cell, which exhibits stable cycling and high discharge capacity.

Origin of superior electrochemical performance

The underlying origin of the exceptional electrochemical performance of $Li_2In_{1/3}Sc_{1/3}Cl_4$ lies in its intrinsically high oxidation stability and high ductility. All lithium metal chlorides should exhibit similar thermodynamic oxidation potentials of 4.21–4.25 V versus Li$^+$/Li on the basis of theory[20]; and, in principle, ASSBs utilizing chloride SEs with similar ionic conductivity should also exhibit comparable electrochemical properties. However, previously reported ASSBs with chloride SEs[19,22–25] exhibit poorer performance than we describe above, suggesting that other factors, including the CAM:SE ratio, cathode composite fabrication and cell pressure, could play an important role.

Figure 6a–c shows the EIS spectra, which monitor the internal resistance evolution of an NCM622 ASSB cycled between 2.8 and 4.6 V during the 1st cycle. The points on the voltage profile where the spectra were collected are indicated. The semicircles in the Nyquist plots represent the overlapping charge transfer contributions from the SE–cathode (and anode) interfaces. On charging
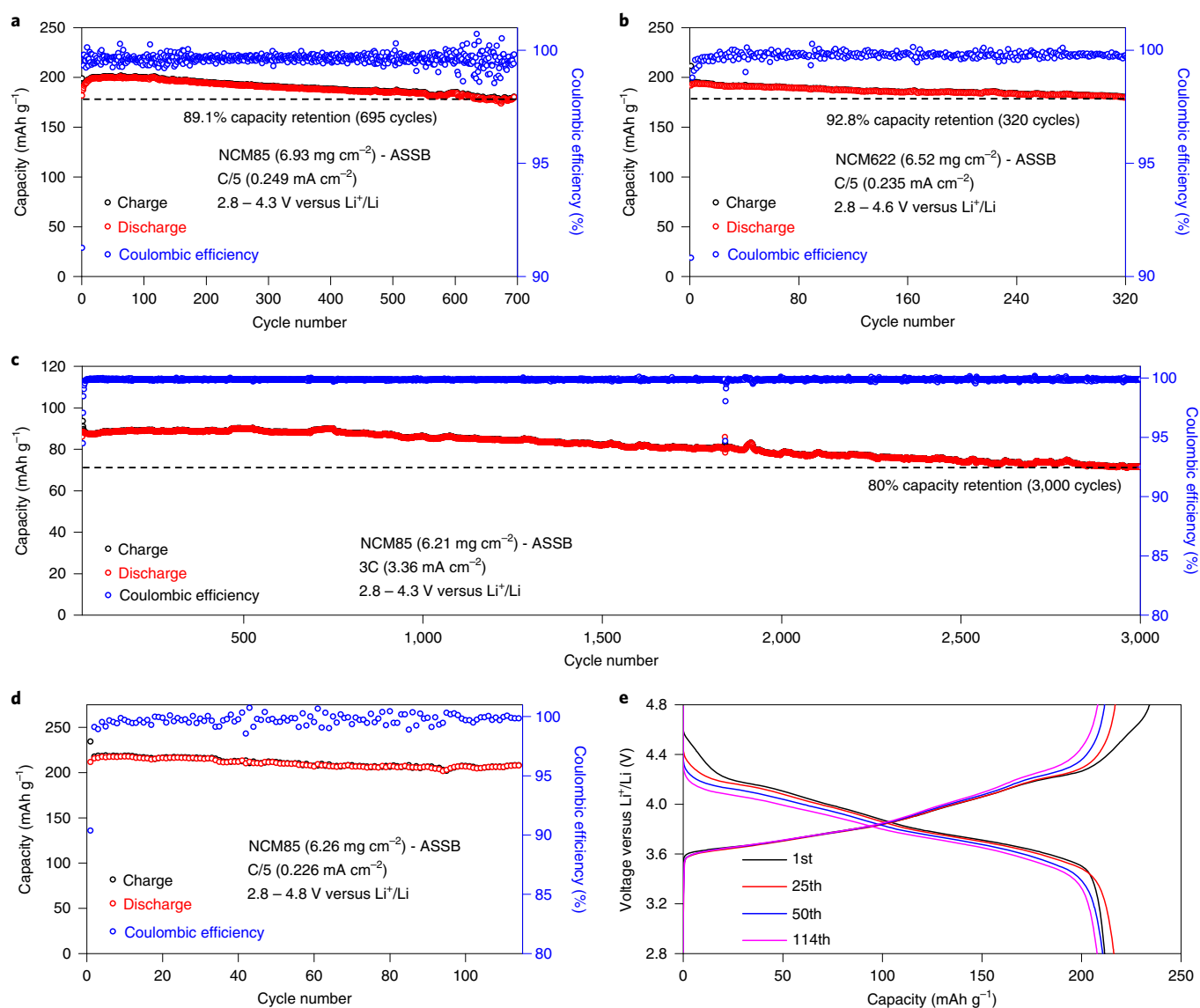
Fig. 4 | Long-term and high-voltage electrochemical performance of ASSBs. a,b, Charge–discharge capacity and the coulombic efficiency (CE) as a function of cycle number for NCM85 ASSB (**a**) and NCM622 ASSB (**b**). **c–e,** Long-term cycling of the NCM85 ASSB (performed after rate cycling) at a 3C rate (**c**) and ultra-high voltage NCM85 ASSB cycled between 2.8 and 4.8 V versus Li$^+$/Li (**d**) and the corresponding charge–discharge voltage profile (**e**).

(Fig. 6b), the cell resistance decreases slightly to reach a minimum at 50% state of charge (SOC) (point 4) and then maximizes at 100% SOC (point 7). While the changes are small, they can be ascribed to changes in the electronic[40] and ionic[41] conductivity of Li$_{1-x}$Ni$_{0.6}$Co$_{0.2}$Mn$_{0.2}$O$_2$ during delithiation. On discharge (Fig. 6c), the process reverses (points 7–11). The much higher impedance at the lowest frequency (100 mHz) for the fully discharged cell (point 12) and at point 1 (Supplementary Fig. 14) is attributed to diffusion limitation in the bulk NCM particles in their reduced state[41]. The same processes were observed for NCM85 and LCO, as shown in Supplementary Figs. 15 and 16. Overall, the total cell resistance is very low during cycling (<80 Ω). Nyquist plots for NCM622 (Fig. 6d; 2.8–4.6 V versus Li$^+$/Li) and LCO (Supplementary Fig. 17; 2.8–4.3 V versus Li$^+$/Li) ASSBs collected at the fully discharged state for cells cycled at C/5 or C/2 show negligible internal resistance increase over 10 cycles. Long-term EIS measurements were conducted for NCM85 ASSBs on charge to 4.3 V, and the corresponding Nyquist plots in Fig. 6e show no internal resistance increase over 160 cycles. This is in accord with a recent finding that

transmission electron microscopy images did not show any change of LiNi$_{0.88}$Co$_{0.11}$Al$_{0.01}$O$_2$ surfaces in contact with a chloride SE cycled to 4.3 V versus Li$^+$/Li[42]. Such remarkably stable impedance confirms the high oxidation stability of chloride SE (up to 4.6 V versus Li$^+$/Li), which allows the use of bare CAMs.

To evaluate interphase growth between NCM85 and SE at a higher potential of 4.8 V versus Li$^+$/Li, the impedance was also monitored at numerous points during the first charge–discharge cycle, and showed excellent reversibility (Supplementary Fig. 18). An accelerated degradation test was conducted by charging the cell to 4.8 V versus Li$^+$/Li and holding for an extended period. The 4.8 V ageing-test leakage current (Fig. 7a) quickly decreased to reach a minimum value of <1 μA at the end of a 30 hour hold, which suggests a very stable interface is formed between NCM85 and Li$_2$In$_{1/3}$Sc$_{1/3}$Cl$_4$. The EIS data (Supplementary Fig. 19a) show a continuous increase of cell impedance during this process and a final charge transfer resistance of 31 kΩ (Supplementary Fig. 19b), caused by the very large drop in Li-ion mobility[41] and electronic conductivity in highly delithiated NCM85 (estimated here to be
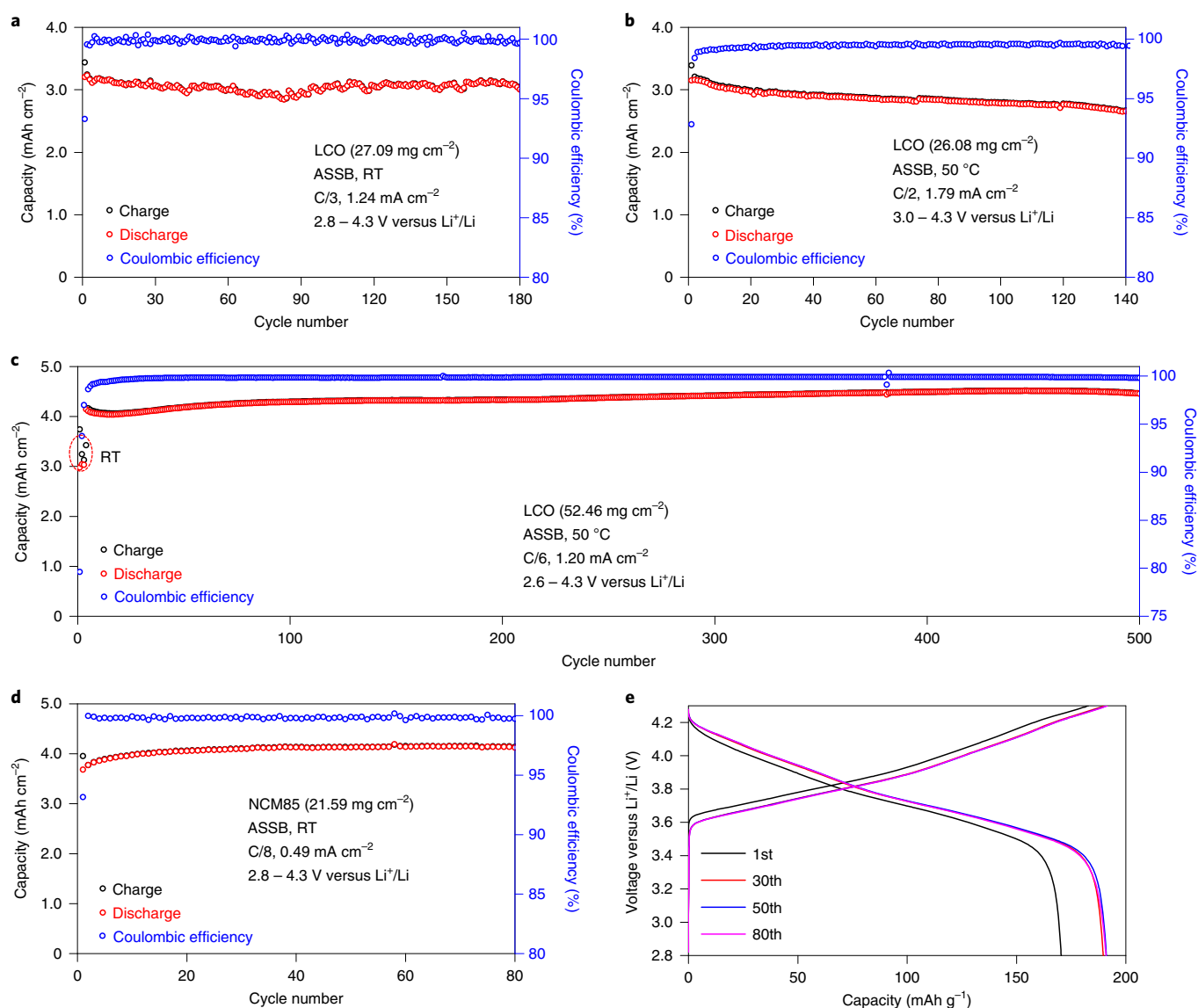
Fig. 5 | High-loading ASSB electrochemical performance. a,b, Charge–discharge capacity and CE as a function of cycle number for LCO ASSBs with areal capacity >3.5 mAh cm^{-2} cycled at room temperature (RT) between 2.8 and 4.3 V versus Li$^+$/Li at C/3 (1.24 mA cm^{-2}) (**a**) and at 50 °C between 3.0 and 4.3 V versus Li$^+$/Li at C/2 (1.79 mA cm^{-2}) (**b**). **c–e,** Ultra-high-loading LCO ASSB with 52.46 mg cm^{-2} loading, cycled at RT between 2.6 and 4.4 V versus Li$^+$/Li and at 50 °C between 2.6 and 4.3 V versus Li$^+$/Li at C/6 (1.20 mA cm^{-2}) (**c**) and high-loading NCM85 ASSB with 21.59 mg cm^{-2} loading cycled at room temperature between 2.8 and 4.3 V versus Li$^+$/Li at C/8 (0.49 mA cm^{-2}) (**d**) and the corresponding charge–discharge curves (**e**). A wider cut-off potential window was used for high-loading ASSBs cycled at RT than at 50 °C owing to the higher overpotential incurred at these current densities (due to limited kinetics of Li-ion/electron diffusion in the thick cathode composite; see Supplementary Fig. 11 for details).

Li$_{0.07}$Ni$_{0.85}$Co$_{0.1}$Mn$_{0.05}$O$_2$). We note that if this impedance originated from the decomposition of Li$_2$In$_{1/3}$Sc$_{1/3}$Cl$_4$ at high voltage, the cell would show significantly increased overpotential and decreased capacity in the following cycles; that is not observed, however. Stable cycling (Fig. 7b) after ageing, and low impedance (Fig. 7c) after final discharge, confirms the existence of a stable interface between NCM85 and Li$_2$In$_{1/3}$Sc$_{1/3}$Cl$_4$ even at 4.8 V versus Li$^+$/Li. A similar stable interface was observed for cells aged at 4.3 V and 4.6 V versus Li$^+$/Li (Supplementary Figs. 20 and 21).

Interface stability is further confirmed by time-of-flight secondary-ion mass spectrometry (TOF-SIMS) surface analysis (Fig. 7d–f and Supplementary Figs. 22–24). TOF-SIMS is highly sensitive even to small fractions of components, and it has recently been shown that SE degradation at the SE/CAM interface and thin coatings can be well analysed[14,43]. Cathode composites cycled

to different cut-off potentials (4.3 V, 4.6 V and 4.8 V versus Li$^+$/Li) were compared to an uncycled cathode composite and the pristine SE. The ClO$^-$ and ScO$^-$ fragments could be a sign of the decomposition of Li$_2$In$_{1/3}$Sc$_{1/3}$Cl$_4$ and reaction with lattice oxygen from NCM at high voltage. However, both signals (Fig. 7e,f) exhibit no obvious increase after cycling compared to the uncycled composite. This indicates minimal reaction of chloride SE occurs with NCM— even up to 4.8 V versus Li$^+$/Li—as a result of a kinetic overpotential due to the extremely low electronic conductivity (4.7 × 10^{-10} S cm^{-1}) of Li$_2$In$_{1/3}$Sc$_{1/3}$Cl$_4$. The presence of ClO$^-$ and ScO$^-$ signals in Li$_2$In$_{1/3}$Sc$_{1/3}$Cl$_4$ and uncycled composite may well originate from impurities in the synthesis of Li$_2$In$_{1/3}$Sc$_{1/3}$Cl$_4$, as residual H$_2$O could be present in the precursors and quartz tube. The slightly increased signal in the uncycled composite compared to pristine SE could originate either from the residual H$_2$O or Li$_2$CO$_3$ contamination on
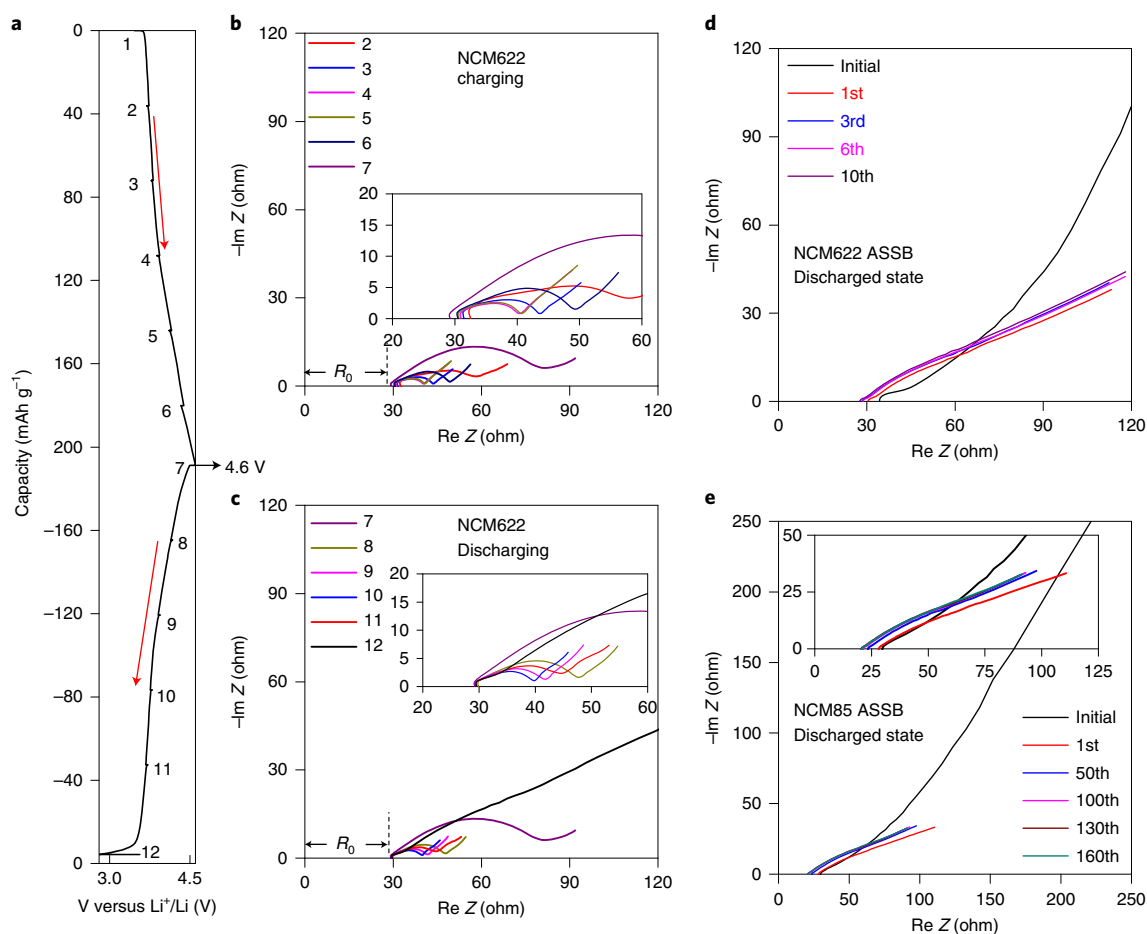
Fig. 6 | ASSB cell impedance evolution during cycling at a C/5 rate. a–c, Impedance evolution during the first cycle of an NCM622 ASSB cycled between 2.8 and 4.6 V versus Li⁺/Li. The corresponding voltage profile (**a**) and impedance spectra collected during charging (**b**) and discharging (**c**) are shown. The numbers on the voltage profile correspond to the points where the EIS spectra were collected at every hour after a 30 min rest (before and after). **d,e**, Nyquist plots of an NCM622 ASSB cycled between 2.8 and 4.6 V versus Li⁺/Li for 10 cycles at full discharge, cells were equilibrated for 1 h before and after (**d**), and an NCM85 ASSB cycled between 2.8 and 4.3 V versus Li⁺/Li for 160 cycles and equilibrated at full discharge for 1 h before and after (**e**). The long diffusion tail in the initial spectrum disappears on subsequent discharge because the pristine state is not attained on Li re-insertion.

the surface of NCM85 particles, as well as from a slightly higher formation rate of secondary ions in the presence of electronically conducting NCM. We point to the much higher and also unchanged signal of Cl⁻ ions, which also supports the stability of the SE at the interface with NCM.

Sulfide SEs, on the other hand, require a CAM coating layer with low electronic and high ionic conductivity to prevent electrolyte oxidation. LiNbO₃ is the commonly used material[43,44]. It is electronically insulating (10^{-11} S cm⁻¹) and a poor ion conductor (~10^{-6} S cm⁻¹)[45]. These properties nonetheless present challenges for cathode design because the low Li-ion conductivity limits Li-ion transfer at the CAM/SE interface (Fig. 8a). Not only is it difficult for the thin coating to homogeneously cover the CAM particles, but also the layer can rupture during fabrication of the cathode composite. Partial electronic conduction through cathode particles can thus occur, and trigger sulfide SE oxidation[46–48]. In contrast, the high potential limit of chloride SEs means bare CAMs can be used, which takes advantage of their inherently high electronic and ionic conductivity. Cathode composites with a high volume ratio of CAM/SE provide direct electronic and Li-ion percolation pathways between CAM particles (Fig. 8a). Due to the high deformability of the chloride SE, simply grinding it with the CAM coats the cathode surface. By controlling the volume ratio between CAM and chloride SE, a

semi-uniform, patchy, thin SE coating on the CAM is obtained, as revealed by scanning electron microscopy (SEM) images (Fig. 8b,c) and energy-dispersive X-ray spectroscopy (EDX) maps (Fig. 8d) of Li₂In₁/₃Sc₁/₃Cl₄-coated NCM85. Supplementary Figs. 25 and 26 show the same for other CAMs (LCO and NCM622). While the high ionic conductivity of the halide coating provides excellent transport of Li-ions in/out of the CAM, importantly, its low electronic conductivity prevents electron leakage from the SE that would result in degradation. More stable cycling is observed when the SE exhibits lower electronic conductivity[27]. The decomposition (oxidation) of any SE at high voltage can only occur via electron diffusion through the interface between the SE and NCM, while a sharp electrochemical potential drop at the interphase layer will prevent this[49]. As Li₂In₁/₃Sc₁/₃Cl₄ exhibits a very low σ_e/σ_i ratio of ~10^{-7}, its oxidation at high voltage is strongly limited by poor electron diffusion. This leads to sluggish kinetics, and thus a higher stability window than predicted by thermodynamics. Such a kinetically driven wider electrochemical stability window is commonly observed for other SEs, such as sulfides (thermodynamic stability ~2.3 V, experimental limit: 2.8–3.1 V versus Li⁺/Li)[12]. Furthermore, when NCM is charged to high voltage (that is, 4.8 V versus Li⁺/Li), the outer surface layer of the NCM particles becomes highly Li-deficient. The significantly lower electronic conductivity (Supplementary
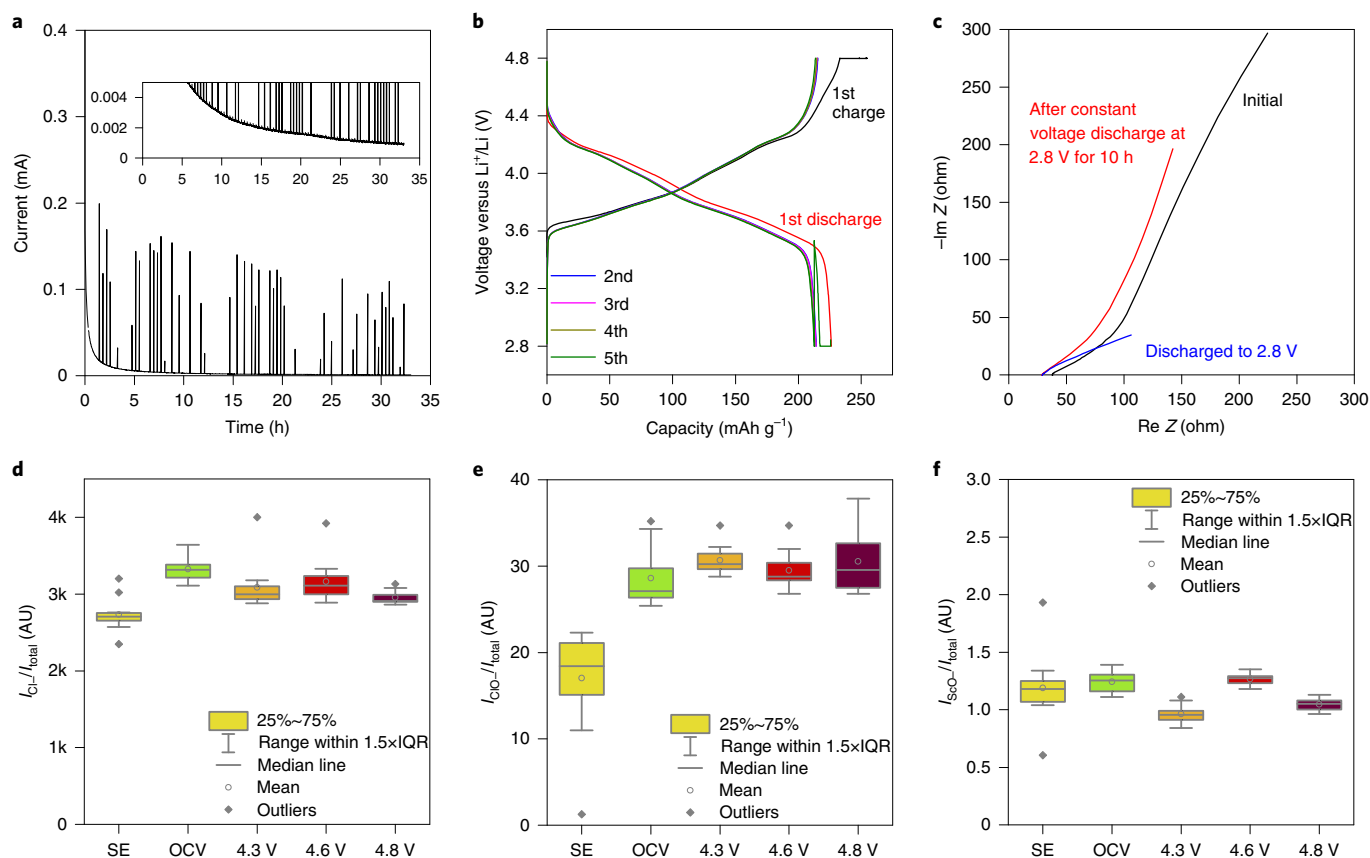
Fig. 7 | Interface evolution between NCM85 and Li$_2$In$_{1/3}$Sc$_{1/3}$Cl$_4$ at high voltage up to 4.8 V versus Li$^+$/Li. a, Leakage current during a hold of NCM85 ASSB at constant voltage of 4.8 V versus Li$^+$/Li after first charge (ageing test). **b**, Charge–discharge voltage profile of NCM85 ASSB. After initial charge, the cell was aged at 4.8 V versus Li$^+$/Li for 30 hours, followed by continuous cycling after ageing. **c**, Nyquist plots of NCM85 ASSB at the initial state, after 5th discharge and after cell discharge held at 2.8 V versus Li$^+$/Li for 10 h. **d–f**, TOF-SIMS surface analysis results of Cl$^-$ (**d**), ClO$^-$ (**e**) and ScO$^-$ (**f**) fragments of bare SE, uncycled cathode composite (OCV) and cycled composites with cut-off potentials of 4.3 V (160 cycles), 4.6 V (20 cycles) and 4.8 V (10 cycles) versus Li$^+$/Li, at a discharged state. The box plots were obtained on the basis of the corresponding normalized signal intensities of 12 spectra on each sample. Box plot centre line represents the median (of median F1 scores); lower and upper box limits represent the 25% and 75% quantiles, respectively; whiskers extend to box limit ±1.5×IQR; outlying points plotted individually. The minima, maxima, median, bounds of box and whiskers, and percentile are provided in Supplementary Table 8.

Fig. 19b) that results further limits the decomposition of SE at high voltage. Nonetheless, because of the low SE:CAM ratio, contact of the residual bare CAM surfaces still provides an electronic conduit between the particles. Thus, an optimal 3D interconnected mixed ionic/electronic network is realized, which is essential for ASSB performance. Operation of the cell under external pressure is necessary to maintain the network on cycling (Supplementary Figs. 27 and 28), since volume expansion/contraction of the CAM particles will otherwise lead to loss of contact of CAM/SE and increasing cell internal resistance[50]. However, high-Ni content CAMs, such as NCM85, still inevitably form cracks and voids on extended cycling that slowly degrade the contact, although over 80% capacity retention can still be maintained over 3,000+ cycles (Fig. 4c). While recognizing that a high applied pressure is not practical in commercial cells, the pressure required partly depends on the nature of the CAM. Hence the development of new CAMs that exhibit minimal volume change on redox along with high ionic/electronic conductivity is important. Future studies also need to probe more precisely how low partial electronic conductivity benefits solid electrolytes by increasing their electrochemical (kinetic) oxidative stability.

Conclusions
A lithium mixed-metal chloride family of SEs, Li$_2$In$_x$Sc$_{0.666-x}$Cl$_4$, exhibits high ionic conductivity up to 2.0 mS cm^{-1} over a wide compositional range. The Li$_2$In$_{1/3}$Sc$_{1/3}$Cl$_4$ spinel exhibits low electronic

conductivity of 4.7×10^{-10} S cm^{-1}, which is one order of magnitude lower than that of Li$_2$Sc$_{2/3}$Cl$_4$, and contributes to its stability at high voltage. Excellent electrochemical performance is demonstrated for bulk-type ASSBs with Li$_2$In$_{1/3}$Sc$_{1/3}$Cl$_4$ in combination with bare-LCO, NCM622 and NCM85 at potentials up to 4.8 V versus Li$^+$/Li. EIS and TOF-SIMS results indicate a stable interface exists between CAMs and chloride SE, confirming the high oxidation stability and chemical compatibility of Li$_2$In$_{1/3}$Sc$_{1/3}$Cl$_4$ in contact with uncoated oxide CAMs. These cells show long cycle life, maintaining 80% capacity retention at high current densities (3.36 mA cm^{-2}; 3C rate) over more than 3,000 cycles. These promising properties are in part due to the high plasticity of the chloride SE, which allows a semi-uniform thin coating on CAM particles to be obtained by gentle grinding. The residual bare surface facilitates electron transport between cathode particles. Incorporation of the SE in the cathode composite (between 10 and 20 wt%) thus provides a 3D interconnected mixed ionic/electronic network within the cathode composite. The applied pressure ensures good CAM/SE contact during long-term cycling, which is essential for ASSB performance. Thus, ASSBs with high CAM loading (up to 52.5 mg cm^{-2} of LCO) deliver stable capacity retention. NCM85 cells are also realized with high areal capacity (>4 mAh cm^{-2}), high specific capacity (>190 mAh g^{-1}) and good cycling behaviour, even at a high cut-off potential of 4.8 V versus Li$^+$/Li. Further developments that will translate the concepts to more earth-abundant and cost-effective
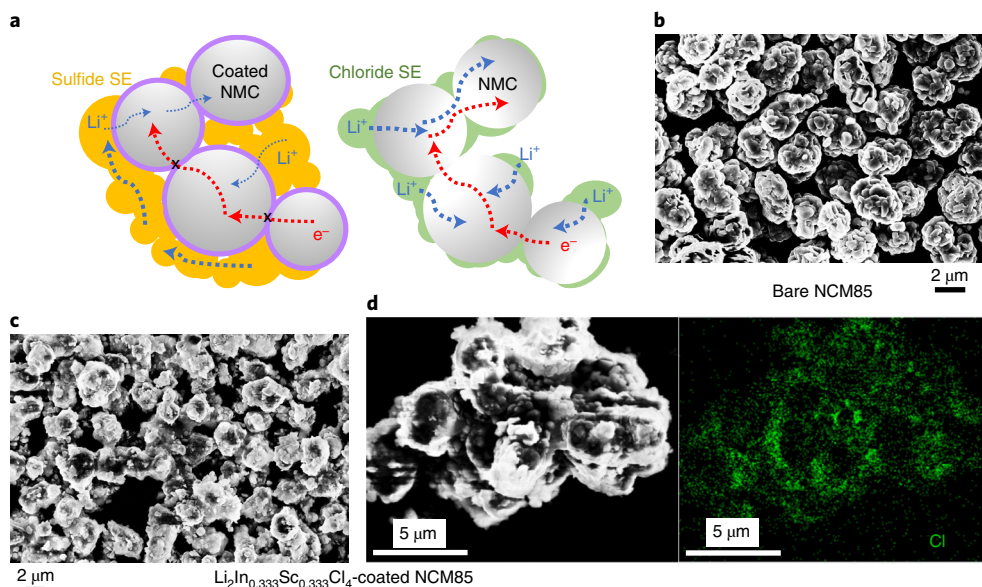
Fig. 8 | Ionic and electronic percolation within cathode composite. a, Schematic illustration of ionic and electronic conduction percolation within a cathode composite of LiNbO$_3$-coated NCM with a sulfide solid electrolyte, and bare NCM with a chloride solid electrolyte. With the poorly conductive (e$^-$/Li$^+$) LiNbO$_3$ coating, both electronic and ionic conductivity between NCM particles are significantly blocked. However, for uncoated NCM and the chloride solid electrolyte, direct contact between NCM particles provides sufficient electronic percolation; combined with Li-ion diffusion through the solid electrolyte and within the NCM particles, conduction within the cathode composite is considerably enhanced. Red arrows show e$^-$ conduction between NCM particles, and black crosses indicate blockage of conduction. Blue arrows show Li$^+$ conduction between NCM particles and between NCM particles and SE and within SE (the thinner blue arrows on the left indicate poor Li$^+$ conduction owing to the low ionic conductivity coating of LiNbO$_3$). **b,c**, SEM images of bare NCM85 (**b**) and Li$_2$In$_{1/3}$Sc$_{1/3}$Cl$_4$-coated NCM85 (**c**) after grinding. **d**, Expanded SEM image of Li$_2$In$_{1/3}$Sc$_{1/3}$Cl$_4$-coated NCM85 with EDX mapping of Cl demonstrates the presence of the chloride solid electrolyte on the surface of NCM85 particles.

lithium metal chloride SEs—and fluoride SEs for next-generation 5 V cells—are anticipated, along with advances in cell design and architecture. These can potentially meet the growing demand for next-generation energy-storage systems for applications such as electric mobility.

Methods

Solid electrolyte synthesis. A simple approach based on mixing and heating of the precursors was used. Stoichiometric amounts of LiCl (Sigma-Aldrich, 99.9%), InCl$_3$ (Alfa Aesar, 99.99%) and ScCl$_3$ (Strem Chemical, 99.99%) were combined at the targeted ratio, pelletized and placed in a sealed quartz tube under vacuum. The pellet was heated to 650 °C at a heating rate of 5 °C min^{-1} and sintered at 650 °C for 48 hours, then slowly cooled to room temperature at 10 °C h^{-1}. Li$_2$Sc$_{2/3}$Cl$_4$ was synthesized as described in our previous paper[26].

X-ray and neutron powder diffraction and structure resolution. Powder X-ray diffraction measurements were conducted at room temperature on a PANalytical Empyrean diffractometer employing CuKα radiation, and the diffractometer was equipped with a PIXcel bidimensional detector. X-ray diffraction patterns were obtained in Bragg–Brentano geometry, with samples placed on a zero-background sample holder in an Ar-filled glovebox and protected by a Kapton film. Selected compositions were measured in Debye–Scherrer geometry with high resolution and long scan times to identify trace impurities, with samples sealed in 0.3 mm (diameter) glass capillaries under argon.

TOF powder neutron diffraction data were collected on POWGEN at the Spallation Neutron Source at Oak Ridge National Laboratory. The sample (~1 g) was loaded into a vanadium can under an argon atmosphere and sealed with a copper gasket and aluminium lid. The sample was measured at 300 K, and a single bank wave with a centre wavelength of 1.5 Å was used. Structure analysis was performed using the TOPAS v.6 software package.

Ionic conductivity and activation energy measurements. The ionic conductivity was measured by EIS. Typically, ~250 mg of the solid electrolyte powder was placed between two stainless steel rods and pressed into a 10 mm diameter pellet by a hydraulic press at 3 tons for 1 min in an Ar-filled glovebox. EIS experiments were performed with 100 mV constant voltage within a frequency range of 1 MHz to 100 mHz using a VMP3 potentiostat/galvanostat (BioLogic). For activation

energy measurements, ~260 mg of the solid electrolyte powder was placed between two stainless steel rods and pressed into a 10 mm diameter pellet by a hydraulic press at 3 tons for 3 min in a custom-made cell, and the cell was then kept in a custom-made cage to maintain a pressure of ~250 MPa. The impedance was measured from 35 MHz to 100 mHz at temperatures ranging from 30 to 60 °C using an MTZ-35 impedance analyser (BioLogic).

Electrochemical measurements. ASSBs employing the Li$_2$In$_{1/3}$Sc$_{1/3}$Cl$_4$ solid electrolyte in combination with a LiCoO$_2$ (LCO, Wellcos, D_{50} = 16.2 μm), LiNi$_{0.6}$Co$_{0.2}$Mn$_{0.2}$O$_2$ (NCM622, BASF, D_{50} = 5 μm) or LiNi$_{0.85}$Co$_{0.1}$Mn$_{0.05}$O$_2$ (NCM85, BASF, D_{50} = 5 μm) cathode active material and a In/InLi anode were assembled in an argon-filled glovebox. All cathode active materials were stored in Ar-filled glovebox and used as received without any treatment. Li$_{6.7}$Si$_{0.7}$Sb$_{0.3}$S$_5$I was synthesized following our previously reported procedure[34]. First, ~100 mg of Li$_{6.7}$Si$_{0.7}$Sb$_{0.3}$S$_5$I powder was placed into a PEEK cylinder and pressed at 2 tons for 1 min (10 mm diameter), and then ~40 mg of Li$_2$In$_{1/3}$Sc$_{1/3}$Cl$_4$ was spread over one side of the Li$_{6.7}$Si$_{0.7}$Sb$_{0.3}$S$_5$I pellet and pressed at 2 tons for another 1 min. The composite cathode mixtures were prepared by mixing LCO or NCM622 or NCM85 and Li$_2$In$_{1/3}$Sc$_{1/3}$Cl$_4$ at a weight ratio of 8:2 or 9:1. On the Li$_2$In$_{1/3}$Sc$_{1/3}$Cl$_4$ side of the SE pellet, ~6–9 mg of the composite cathode mixture (corresponding to an areal capacity of ~1.1–1.25 mAh cm^{-2}) was spread and pressed at 3 tons for 3 min. For high-loading cells, ~20–53 mg cathode composite was used, and the corresponding areal capacities are labelled in the figures. On the other side of the pellet, a thin indium foil (10 mm diameter, 99.99%, 0.1 mm thickness) was attached and ~1 mg Li foil (Sigma-Aldrich) was pressed into a thin layer (around 5 mm diameter) and placed over the indium foil. The cell was placed into a custom-made stainless steel casing with a constant applied pressure of ~250 MPa during cycling.

NCM liquid cells were assembled following standard procedures. For electrode fabrication, NCM622 or NCM85 powder was mixed with Super P carbon (Timcal) and polyvinylidene fluoride (Sigma-Aldrich, average M_w ≈ 534,000 GPC) to achieve a final weight ratio of 8:1:1 (active material:carbon:binder). The powdered mixture was then suspended in N-methyl-2-pyrrolidinone (Sigma-Aldrich, 99.5%) to obtain a viscous slurry, which was cast on Al foil with a typical loading of ~3.6 mg cm^{-2}. The electrodes were punched to a 1 cm^2 geometric area and dried in a vacuum oven at 120 °C overnight. Electrochemical studies were carried out in 2325 coin-type half-cells with a Li-metal anode, Celgard 3501 separator and LP57 electrolyte (Gotion, 1 M LiPF$_6$ in ethylene carbonate:ethyl methyl carbonate at a ratio of 3:7).

Galvanostatic cycling of the cell was carried out in different voltage ranges at different rates (as labelled) using a VMP3 (BioLogic) cycler. Rate current density calculations used conventional values for LCO ($1C = 137 \, mA \, g^{-1}$) and NCM622/NCM85 ($1C = 180 \, mA \, g^{-1}$).

ASSBs with LCO, NCM622 and NCM85 CAMs were constructed for impedance measurements following the same procedure as above and cycled at C/5 as indicated. Measurements were conducted after every 1 hour of charge–discharge, before and after which the cells were placed at rest for 30 min. For the impedance measurements after full discharge, the cells were placed at rest for 1 h before and after the measurement.

ASSBs with NCM85 for ageing experiments were constructed following the same procedure. Cells were first charged to 4.3 V, 4.6 V and 4.8 V versus Li^+/Li, respectively, followed by constant potential ageing at 4.3 V, 4.6 V and 4.8 V for 30 h. EIS was conducted every 20 min of ageing with constant applied potentials of 4.3 V, 4.6 V and 4.8 V, and no rest. After ageing, the cells were continuously cycled for several cycles. Then, the final EIS spectra were measured at the discharged state with no constant applied potential and 0.5 h rest after discharge.

TOF-SIMS. Cycled cathode composites $NCM85-Li_2In_{1/3}Sc_{1/3}Cl_4$ (cut-off 4.3 V for 160 cycles, cut-off 4.6 V for 20 cycles and cut-off 4.8 V for 10 cycles) were compared to pristine SE and uncycled cathode composite, and all measurements were conducted at the discharged state. The chemical characterization was performed on a Hybrid TOF-SIMS M6 machine (IONTOF). To transfer the samples from the glovebox into the measurement chamber, the transfer module Leica EM VCT500 (Leica Microsystems) was applied to guarantee an argon atmosphere. The measurements were conducted on the top surface of the cathode composite pellets.

To avoid topographic interference and ensure reproducibility, we measured 12 mass spectra in different areas on each sample. The measurements were carried out in spectrometry mode (bunched mode), which enables a high mass resolution (full-width at half-maximum $m/\Delta m > 7,000$ at m/z 34.97 (Cl^-)). All spectra were collected in negative-ion mode using a 60 keV Bi_3^{++} cluster primary ion gun. The cycle time was set to 100 μs. The measurement area was set to $150 \times 150 \, \mu m^2$ and rasterized with 256×256 pixels. For each patch, 1 frame and 1 shot per pixel and frame were chosen. The primary ion current was about 0.43 pA. To enable the semiquantitative analysis, the stop condition was set with the primary ion dose of 10^{12} ions per cm^2.

The data evaluation was conducted with Surfacelab v.7.2 software (IONTOF). The secondary-ion signals were normalized to the total ion signals, and all signal intensities were collected from the corresponding normalized secondary-ion images.

Scanning electron microscopy. Material morphologies and elemental analysis studies utilized a Zeiss field-emission scanning electron microscope equipped with an EDX detector.

Single-crystal diffraction. The data were collected on a Bruker Kappa diffractometer equipped with a Smart Apex II CCD, utilizing graphite-monochromated MoKα radiation. The crystal was protected by Paratone-N oil and a liquid nitrogen flow using an Oxford Cryostream controller 700 at 270 K, to ensure no reactivity of the materials occurred. The data were collected by scanning ω of 0.3° in a few groups of frames at different ϕ and an exposure time of 60 s per frame (generic omega and phi scans). The data were corrected for Lorentz and polarization effects. Absorption correction was carried out using the empirical multiscan method SADABS, part of the Bruker suite. Cell_Now software was used to check for potential twinning and indexing the unit cell reflections, with I/σ below 5 to check for a possible supercell, but no supercells were observed. The structure was solved by direct methods to locate the positions of In and Cl atoms. First, these positions were anisotropically refined using the least-squares method incorporated in the SHELXTL package. The In site was refined as a mixed In/Sc of around 67% and 33%, respectively. Then, the Li positions were located in the remaining electron density in the Fourier map, which revealed Li–Cl bonds very similar in length to those found in binary and ternary Li chlorides. Subsequently, the Li site occupancies were freely and anisotropically refined except for Li2, which was isotropically refined. The refinement was converged to good residual values $R1 = 0.0365$ and $wR2 = 0.0762$ for all data. The program Tidy was used to standardize the atomic positions. No constraints were used during the structure refinements, except for the In/Sc mixed site.

Data availability

Data generated and analysed in this study are included in the paper and Supplementary Information. The single-crystal X-ray crystallographic data for the structure reported in this study has been deposited at the Cambridge Crystallographic Data Centre under deposition number 2115525. These data can be obtained free of charge from the Cambridge Crystallographic Data Centre via www.ccdc.cam.ac.uk.

References

1. Trahey, L. et al. Energy storage emerging: a perspective from the Joint Center for Energy Storage Research. *Proc. Natl Acad. Sci. USA* **1**, 12550–12557 (2020).
2. Lee, Y. G. et al. High-energy long-cycling all-solid-state lithium metal batteries enabled by silver–carbon composite anodes. *Nat. Energy* **5**, 299–308 (2020).
3. Randau, S. et al. Benchmarking the performance of all-solid-state lithium batteries. *Nat. Energy* **5**, 259–270 (2020).
4. Chen, R., Li, Q., Yu, X., Chen, L. & Li, H. Approaching practically accessible solid-state batteries: stability issues related to solid electrolytes and interfaces. *Chem. Rev.* **120**, 6820–6877 (2020).
5. Zhang, Z. et al. New horizon for inorganic solid state ion conductors. *Energy Environ. Sci.* **11**, 1945–1976 (2018).
6. Bachman, J. C. et al. Inorganic solid-state electrolytes for lithium batteries: mechanisms and properties governing ion conduction. *Chem. Rev.* **116**, 140–162 (2016).
7. Park, K. H. et al. Design strategies, practical considerations, and new solution processes of sulfide solid electrolytes for all-solid-state batteries. *Adv. Energy Mater.* **8**, 1800035 (2018).
8. Balaish, M. et al. Processing thin but robust electrolytes for solid-state batteries. *Nat. Energy* **6**, 227–239 (2021).
9. Kamaya, N. et al. A lithium superionic conductor. *Nat. Mater.* **10**, 682–686 (2011).
10. Kato, T. et al. High-power all-solid-state batteries using sulfide superionic conductors. *Nat. Energy* **1**, 16030 (2016).
11. Zhu, Y., He, X. & Mo, Y. Origin of outstanding stability in the lithium solid electrolyte materials: insights from thermodynamic analyses based on first-principles calculations. *ACS Appl. Mater. Interfaces* **7**, 23685–23693 (2015).
12. Dewald, G. F. et al. Experimental assessment of the practical oxidative stability of lithium thiophosphate solid electrolytes. *Chem. Mater.* **31**, 8328–8337 (2019).
13. Schwietert, T. K. et al. Clarifying the relationship between redox activity and electrochemical stability in solid electrolytes. *Nat. Mater.* **19**, 428–435 (2020).
14. Walther, F. et al. Visualization of the interfacial decomposition of composite cathodes in argyrodite-based all-solid-state batteries using time-of-flight secondary-ion mass spectrometry. *Chem. Mater.* **31**, 3745–3755 (2019).
15. Banerjee, A., Wang, X., Fang, C., Wu, E. A. & Meng, Y. S. Interfaces and interphases in all-solid-state batteries with inorganic solid electrolytes. *Chem. Rev.* **120**, 6878–6933 (2020).
16. Xiao, Y., Miara, L. J., Wang, Y. & Ceder, G. Computational screening of cathode coatings for solid-state batteries. *Joule* **3**, 1252–1275 (2019).
17. Nolan, A. M., Liu, Y. & Mo, Y. Solid-state chemistries stable with high-energy cathodes for lithium-ion batteries. *ACS Energy Lett.* **4**, 2444–2451 (2019).
18. Jung, S. H. et al. $Li_3BO_3-Li_2CO_3$: rationally designed buffering phase for sulfide all-solid-state Li-ion batteries. *Chem. Mater.* **30**, 8190–8200 (2018).
19. Asano, T. et al. Solid halide electrolytes with high lithium-ion conductivity for application in 4 V class bulk-type all-solid-state batteries. *Adv. Mater.* **30**, 1803075 (2018).
20. Wang, S. et al. Lithium chlorides and bromides as promising solid-state chemistries for fast ion conductors with good electrochemical stability. *Angew. Chem. Int. Ed. Engl.* **58**, 8039–8043 (2019).
21. Muy, S. et al. High-throughput screening of solid-state Li-ion conductors using lattice-dynamics descriptors. *iScience* **16**, 270–282 (2019).
22. Li, X. et al. Air-stable Li_3InCl_6 electrolyte with high voltage compatibility for all-solid-state batteries. *Energy Environ. Sci.* **12**, 2665–2671 (2019).
23. Park, K. H. et al. High-voltage superionic halide solid electrolytes for all-solid-state Li-ion batteries. *ACS Energy Lett.* **5**, 533–539 (2020).
24. Kim, S. Y. et al. Lithium ytterbium based halide solid electrolytes for high voltage all-solid-state batteries. *ACS Mater. Lett.* **3**, 930–938 (2021).
25. Liang, J. et al. Site-occupation-tuned superionic Li_xScCl_{3+x} halide solid electrolytes for all-solid-state batteries. *J. Am. Chem. Soc.* **142**, 7012–7022 (2020).
26. Zhou, L. et al. A new halospinel superionic conductor for high-voltage all solid state lithium batteries. *Energy Environ. Sci.* **13**, 2056–2063 (2020).
27. Kwak, H. et al. New cost-effective halide solid electrolytes for all-solid-state batteries: mechanochemically prepared Fe^{3+}-substituted Li_2ZrCl_6. *Adv. Energy Mater.* **11**, 2003190 (2021).
28. Park, J. et al. Heat treatment protocol for modulating ionic conductivity via structural evolution of $Li_{3-x}Yb_{1-x}M_xCl_6$ ($M = Hf^{4+}$, Zr^{4+}) new halide superionic conductors for all-solid-state batteries. *Chem. Eng. J.* **425**, 130630 (2021).
29. Kato, Y. et al. All-solid-state batteries with thick electrode configurations. *J. Phys. Chem. Lett.* **9**, 607–613 (2018).
30. Minnmann, P., Quillmann, L., Burkhardt, S., Richter, F. H. & Janek, J. Quantifying the impact of charge transport bottlenecks in composite cathodes of all-solid-state batteries. *J. Electrochem. Soc.* **168**, 040357 (2021).
31. Liu, H. et al. Elucidating the limit of Li insertion into the spinel $Li_4Ti_5O_{12}$. *ACS Mater. Lett.* **1**, 96–102 (2019).

32. Zhang, W. et al. Kinetic pathways of ionic transport in fast-charging lithium titanate. *Science* **367**, 1030–1034 (2020).

33. Bohnsack, A. et al. Ternary halides of the A_3MX_6 type. Part VI. Ternary chlorides of the rare-earth elements with lithium, Li_3MCl_6 (M = Tb-Lu, Y, Sc): synthesis, crystal structures, and ionic motion. *Z. Anorg. Allg. Chem.* **623**, 1067–1073 (1997).

34. Zhou, L. et al. New family of argyrodite thioantimonate lithium superionic conductors. *J. Am. Chem. Soc.* **141**, 19002–19013 (2019).

35. Xue, W. et al. Ultra-high-voltage Ni-rich layered cathodes in practical Li metal batteries enabled by a sulfonamide-based electrolyte. *Nat. Energy* **6**, 495–505 (2021).

36. Shi, T. et al. High active material loading in all-solid-state battery electrode via particle size optimization. *Adv. Energy Mater.* **10**, 1902881 (2019).

37. Strauss, F. et al. Impact of cathode material particle size on the capacity of bulk-type all-solid-state batteries. *ACS Energy Lett.* **3**, 992–996 (2018).

38. Han, F. et al. Interphase engineering enabled all-ceramic lithium battery. *Joule* **2**, 497–508 (2018).

39. Kubanska, A., Castro, L., Tortet, L., Dollé, M. & Bouchet, R. Effect of composite electrode thickness on the electrochemical performance of all-solid-state Li-ion batteries. *J. Electroceram.* **38**, 189–196 (2017).

40. Amin, R. & Chiang, Y. M. Characterization of electronic and ionic transport in in $Li_{1-x}Ni_{0.33}Mn_{0.33}Co_{0.33}O_2$ (NMC333) and $Li_{1-x}Ni_{0.50}Mn_{0.20}Co_{0.30}O_2$ (NMC523) as a function of Li content. *J. Electrochem. Soc.* **163**, A1512 (2016).

41. Märker, K. et al. Evolution of structure and lithium dynamics in $LiNi_{0.8}Mn_{0.1}Co_{0.1}O_2$ (NMC811) cathodes during electrochemical cycling. *Chem. Mater.* **31**, 2545–2554 (2019).

42. Han, Y. et al. Single- or poly-crystalline Ni-rich layered cathode, sulfide or halide solid electrolyte: which will be the winner for all-solid-state batteries? *Adv. Energy Mater.* **11**, 2100126 (2021).

43. Walther, F. et al. The working principle of a $Li_2CO_3/LiNbO_3$ coating on NCM for thiophosphate-based all-solid-state batteries. *Chem. Mater.* **33**, 2110–2125 (2021).

44. Ohta, N. et al. $LiNbO_3$-coated $LiCoO_2$ as cathode material for all solid-state lithium secondary batteries. *Electrochem. Commun.* **9**, 1486–1490 (2007).

45. Glass, A. M., Nassau, K. & Negran, T. J. Ionic conductivity of quenched alkali niobate and tantalate glasses. *J. Appl. Phys.* **49**, 4808 (1978).

46. Strauss, F. et al. Li_2ZrO_3-coated NMC622 for application in inorganic solid-state batteries: role of surface carbonates in the cycling performance. *ACS Appl. Mater. Interfaces* **12**, 557146–557154 (2020).

47. Banerjee, A. et al. Revealing nanoscale solid–solid interfacial phenomena for long-life and high-energy all-solid-state batteries. *ACS Appl. Mater. Interfaces* **11**, 443138–43135 (2019).

48. Zhang, Y. Q. et al. Direct visualization of the interfacial degradation of cathode coating in solid state batteries: a combined experimental and computational study. *Adv. Energy Mater.* **10**, 1903778 (2020).

49. Nakamura, T. et al. Guidelines for all-solid-state battery design and electrode buffer layers based on chemical potential profile calculation. *ACS Appl. Mater. Interfaces* **11**, 19968–19976 (2019).

50. Koerver, R. et al. Chemo-mechanical expansion of lithium electrode materials—on the route to mechanically optimized all-solid-state batteries. *Energy Environ. Sci.* **11**, 2142–2158 (2018).

Acknowledgements

Author contributions

L.Z. and L.F.N. conceived and designed the experimental work. L.Z. performed the synthesis of the solid electrolytes, powder X-ray diffraction measurements, structural resolution of powder neutron diffraction and the electrochemistry of all-solid-state batteries. T.-T.Z. performed the TOF-SIMS measurements, and data analysis was performed by T.T.Z. and J.J. C.Y.K. performed the SEM measurements. S.Y.K. performed the electrochemistry of liquid NCM cells. A.A. performed single-crystal diffraction and structure resolution. Q.Z. performed the powder neutron diffraction measurements. L.Z. and L.F.N. wrote the manuscript with input from all authors.

Competing interests

The authors declare no competing interests.

Additional information